

Transit least-squares survey

II. Discovery and validation of 17 new sub- to super-Earth-sized planets in multi-planet systems from *K2*

René Heller¹, Michael Hippke², and Kai Rodenbeck^{3,1}

¹ Max Planck Institute for Solar System Research, Justus-von-Liebig-Weg 3, 37077 Göttingen, Germany, heller@mps.mpg.de

² Sonneberg Observatory, Sternwartestraße 32, 96515 Sonneberg, Germany, michael@hippke.org

³ Inst. for Astrophysics, Georg-August-Univ. Göttingen, Friedrich-Hund-Platz 1, 37077 Göttingen, Germany, rodenbeck@mps.mpg.de

Received 2 April 2019; Accepted 13 May 2019

ABSTRACT

The extended *Kepler* mission (*K2*) has revealed more than 500 transiting planets in roughly 500 000 stellar light curves. All of these were found either with the box least-squares algorithm or by visual inspection. Here we use our new transit least-squares (TLS) algorithm to search for additional planets around all *K2* stars that are currently known to host at least one planet. We discover and statistically validate 17 new planets with radii ranging from about 0.7 Earth radii (R_{\oplus}) to roughly $2.2 R_{\oplus}$ and a median radius of $1.18 R_{\oplus}$. EPIC 201497682.03, with a radius of $0.692^{+0.059}_{-0.048} R_{\oplus}$, is the second smallest planet ever discovered with *K2*. The transit signatures of these 17 planets are typically 200 ppm deep (ranging from 100 ppm to 2000 ppm), and their orbital periods extend from about 0.7 d to 34 d with a median value of about 4 d. Fourteen of these 17 systems only had one known planet before, and they now join the growing number of multi-planet systems. Most stars in our sample have subsolar masses and radii. The small planetary radii in our sample are a direct result of the higher signal detection efficiency that TLS has compared to box-fitting algorithms in the shallow-transit regime. Our findings help in populating the period-radius diagram with small planets. Our discovery rate of about 3.7% within the group of previously known *K2* systems suggests that TLS can find over 100 additional Earth-sized planets in the data of the *Kepler* primary mission.

Key words. eclipses – methods: data analysis – planets and satellites: detection – stars: planetary systems – techniques: photometric

1. Introduction

After the continuous monitoring of its prime observing field from 2009 to 2013, the repurposed *Kepler* telescope (Borucki et al. 2010) performed another 19 campaigns of different target fields along the ecliptic, covered for about 75 d each from 2014 until 2018 (Howell et al. 2014). Although the failure of the second of the four reaction wheels of *Kepler* initially produced degraded photometric precision of the *K2* mission, new decorrelation techniques between photometrically extracted light curves and the telescope pointing (Vanderburg & Johnson 2014; Lund et al. 2015; Aigrain et al. 2016) led to substantial improvements of the noise properties of the light curves. Finally, Luger et al. (2016) constructed EVEREST, an automated *K2* photometric extraction pipeline based on a pixel level decorrelation technique (Deming et al. 2015) in combination with a Gaussian process optimization (Aigrain et al. 2015).

These improvements of the *K2* stellar photometry calibration allowed the confirmation of 359 exoplanets and 472 more candidates¹, in addition to the 2331 confirmed planets and 2425 candidates yet to be confirmed from the *Kepler* primary mission. All *K2* planets and candidates were found using either a direct application of the box least-squares (BLS) (Kovács et al. 2002) transit search algorithm, for example, for the searches by Adams et al. (2016), Vanderburg et al. (2016), Barros et al. (2016), Mann et al. (2016), Gaidos et al. (2017), van Sluijs &

Van Eylen (2018), Livingston et al. (2018b), Mayo et al. (2018), and Giles et al. (2018), or its implementation within the TERRA pipeline (Petigura & Marcy 2012; Petigura et al. 2013), for instance, for the searches by Crossfield et al. (2015, 2016, 2018), Sinukoff et al. (2016), Yu et al. (2018), Livingston et al. (2018a), and Zink et al. (2019), or similar algorithms searching for box-like flux decreases in stellar light curves (Foreman-Mackey et al. 2015) or by eye (Osborn et al. 2016; Schmitt et al. 2016).

The BLS algorithm and its variations (Collier Cameron et al. 2006; Renner et al. 2008; Carter & Agol 2013; Petigura et al. 2013; Ofir 2014; Bouffleur et al. 2014) is certainly the most widely used transit search algorithm, although alternative algorithms exist (Jenkins et al. 1996; Aigrain & Favata 2002; Aigrain & Irwin 2004; Schwarzenberg-Czerny & Beaulieu 2006; Bordé et al. 2007; Régulo et al. 2007; Cabrera et al. 2012). The popularity of BLS is well founded in its good detection efficiency of shallow transits (Tingley 2003a,b) and computational speed, for example, compared to algorithms using artificial intelligence (Mislis et al. 2016; Pearson et al. 2018; Zucker & Giryes 2018; Armstrong et al. 2018).

We recently presented the transit least-squares (TLS) algorithm, which is optimized for the detection of shallow periodic transits (Hippke & Heller 2019). In contrast to BLS, the test function of TLS is not a box, but an analytical model of a transit light curve (Mandel & Agol 2002). As a consequence, the residuals between the TLS search function and the observed data are substantially smaller than the residuals obtained with BLS or

¹ https://exoplanetarchive.ipac.caltech.edu/docs/counts_detail.html on 22 February 2019

similar box-like algorithms, resulting in an enhancement of the signal detection efficiency for TLS, in particular for weak signals.

The advantages of using TLS instead of BLS in searching for small planets were first illustrated by Hippke & Heller (2019) using simulated light curves. These predictions were verified using actual *K2* photometry with the discovery of the Earth-sized planet K2-32 e (Heller et al. 2019, hereafter Paper I) around a star that was known to host three roughly Neptune-sized planets. Here we extend the TLS Survey and present the results of our search for hitherto unknown additional planets around all stars from *K2* that were already known to host at least one planet.

2. Methods

2.1. Target selection

We reanalyzed the 517 *K2* planets and candidates (in 489 unique systems) from the NASA Exoplanet Archive² (Akeson et al. 2013) and the Exoplanet Orbit Database³ (Han et al. 2014), most of which have been discovered by Foreman-Mackey et al. (2015), Vanderburg et al. (2016), Crossfield et al. (2016), Mayo et al. (2018), and Livingston et al. (2018b). We chose these *K2* systems with known planets for this initial phase of the TLS Survey since any additional findings would have an intrinsically low false-positive probability (Lissauer et al. 2012), which simplifies our vetting and validation procedure.

2.2. Transit search

Our methods are in principle the same as described in Paper I. We used the publicly available *K2* light curves after correction for instrumental effects with EVEREST (Luger et al. 2016). Using the published periods, transit durations, and mid-transit times, we removed the in-transit flux of known planets in these systems. Then we removed stellar variability and other trends using a median filter with a window size of 25 long cadences. Each cadence corresponds to an exposure of about 30 min, making the walking window as wide as about half a day. This window size was chosen as a compromise so that it is sufficiently short to remove stellar variability, but leaves transit signals intact. For planets with periods < 80 days, transit durations are shorter in any physically plausible case, and much shorter in almost all cases (Hippke & Heller 2019, Paper I). The longest transit duration of the planets we discover is about 0.21 d. We clipped all data points that are more than 3σ above the running mean in order to remove data points affected by cosmic-ray impacts on the CCD.

After this preprocessing of the light curves, we applied TLS (version 1.0.13) using the stellar limb darkening, mass, and radius estimates available in the EPIC catalog (Huber et al. 2016). For all other TLS parameters we used the default values.

2.3. Vetting

Our vetting process includes an automated detection of transit candidates with TLS and a visual inspection of the light curve together with the derived basic properties of the candidate.

The automated part of the vetting pipeline uses several vetting criteria, the most important of which is the signal detection efficiency of TLS (SDE_{TLS}). As shown by Hippke & Heller (2019), an SDE_{TLS} of 9 would result in a false-positive rate < 10^{-4} in the limiting case of white noise. Of course, *K2* light

curves contain various sources of time-dependent variability so that we expected (and indeed found) a higher false-positive rate. If a candidate exhibited five or fewer transits, then all transits were required to have a temporal separation of at least 0.5 d from the beginning or the end of any gaps in the respective light curve to avoid false positives created by instrumental trends and by the detrending procedures. If a candidate exhibited three or fewer transits, then a signal-to-noise ratio (S/N) > 10 was required, which we computed as $S/N = (\delta/\sigma_o)n^{1/2}$ with δ as the mean transit depth, σ_o as the standard deviation of the out-of-transit points, and n as the number of in-transit data points (Pont et al. 2006).

Furthermore, for all objects we required that the average depth of the odd and even transits agreed within $< 3\sigma$. We also ignored any objects with evidence of a secondary eclipse at the $> 3\sigma$ level compared to the local noise at half an orbital phase after the candidate transit. The latter two conditions were meant to reject eclipsing binaries. In our search for transiting planets, which we suspected to be much smaller than Jupiter or Neptune (because otherwise they would have been found previously), we also rejected any candidates that show signs of phase-curve variations in the vetting sheet. This signature is much more likely to be caused by an eclipsing stellar binary than by an Earth- or super-Earth-sized object.

For any object that passed all our vetting criteria, our pipeline automatically created a vetting sheet that we used for our visual inspection. Figure 1 presents an example, and the panels are explained in the figure caption. The Lomb-Scargle periodograms shown in the bottom panels were computed with the implementation of *astropy*, which makes use of the floating mean periodogram of Zechmeister & Kürster (2009).

2.4. False-positive probabilities

We used the *vespa* software (Morton 2012, 2015) to evaluate the false-positive probability (FPP) for each of our candidates. Details of our usage of *vespa* are given in Paper I. In brief, we used the star's astrophysical characterization, that is, its effective temperature, surface gravity, and metallicity, from the *K2* Ecliptic Plane Input Catalog of Huber et al. (2016) and the astronomical information from the 2MASS broadband photometry (J , H , K ; Cutri et al. 2003). The stellar radii for EPIC 201497682, EPIC 201841433, EPIC 212297394, and EPIC 212499991 listed by Huber et al. (2016) have uncertainties of up to several solar radii. For these objects we used the stellar radii published in the Gaia data release 2 (DR2) (Gaia Collaboration et al. 2016, 2018) as estimated by Andrae et al. (2018) in order to compute the planetary radii from the respective stellar radius and the planet-to-star radius ratio measured with our Markov chain Monte Carlo (MCMC) fitting (see Sect. 2.5).

One critical criterion for the computation of the FPP with *vespa* was the maximum aperture radius (ρ) interior to which the signal must be produced (the *maxrad* parameter in *vespa*). We retrieved and inspected optical images from the Panoramic Survey Telescope and Rapid Response System (Pan-STARRS; Chambers et al. 2016) through the Aladin software to evaluate the possibility of contamination by uncorrelated objects and to determine ρ . Pan-STARRS is complete to visual magnitudes of about 22 with a resolution down to 200 mas per pixel and therefore both sufficiently deep and sufficiently resolved for us to constrain the presence of contaminants. Blurring effects from astronomical seeing and the Pan-STARRS telescope point spread function limited our resolution to a minimum of $\rho \sim 1''$ in those cases where no resolved sources of contamination were visible.

² <https://exoplanetarchive.ipac.caltech.edu>

³ <http://exoplanets.org>

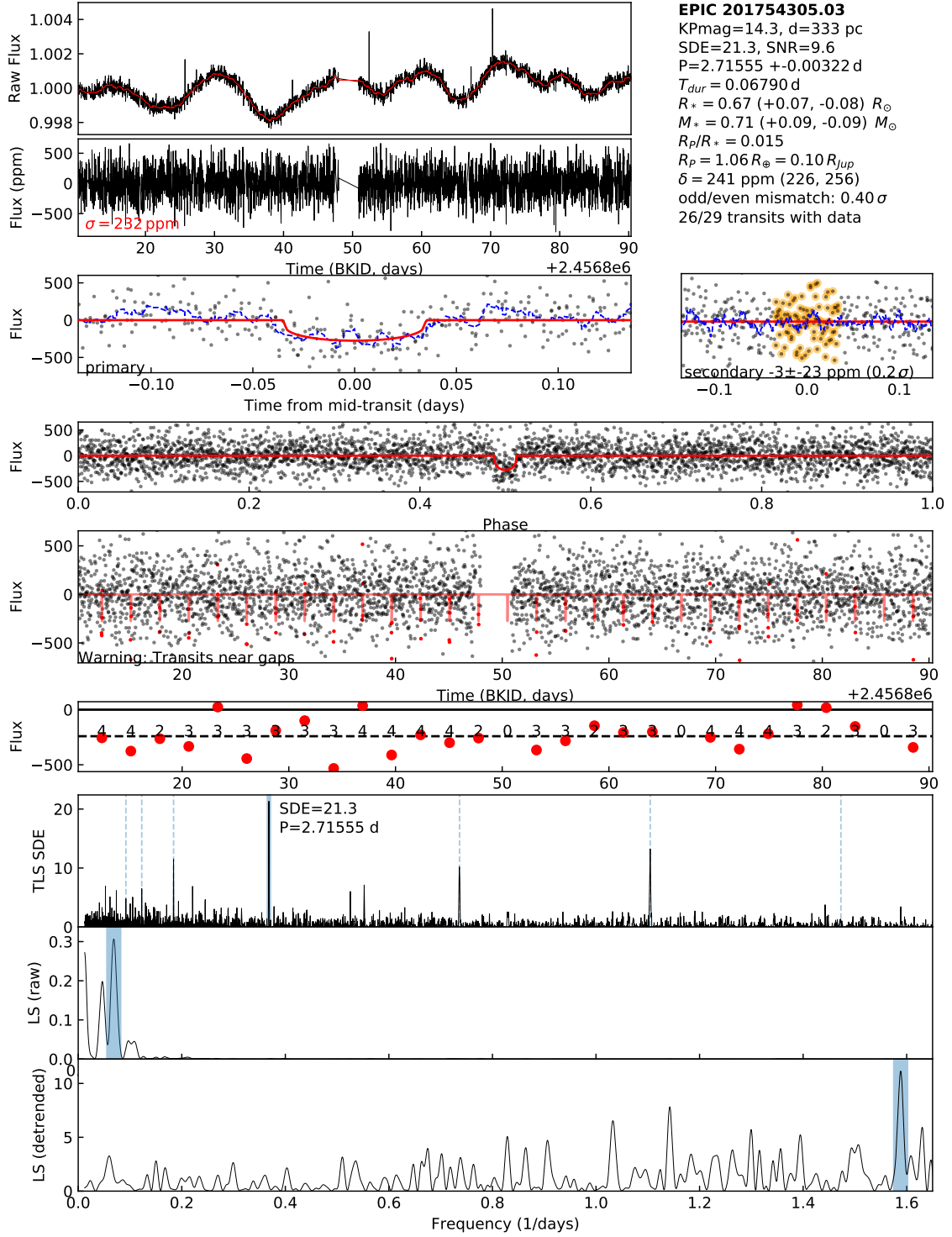


Fig. 1. Example of a vetting sheet, here for 201754305.03. From top to bottom, the panels show the raw flux of the EVEREST light curve (with the running median in red), the normalized light curve, zooms into the transit candidate (left), and possible eclipse (right) times of the phase-folded light curve, the entire phase-folded light curve, the entire light curve with in-transit data of the new candidate marked in red, the sequence of transit depth measurements (including the number of in-transit points), the SDE_{TLS} periodogram, the Lomb-Scargle periodogram of the raw light curve, and the Lomb-Scargle periodogram of the detrended light curve. A summary of the basic system properties is shown in the upper right corner.

One notable exception was EPIC 201754305 (*K2*-16), for which we referred to adaptive optic imaging from Sinukoff et al. (2016) and restricted contamination to within $\rho = 0.5''$.

The *K2* photometric apertures of our targets were typically smaller than about six pixels or $\leq 24''$ given that the spatial resolution of the *K2* CCD is $4''$ per pixel. For all our candi-

dates, we compared the corresponding *K2* Full Frame Images⁴ of the respective *K2* campaign and CCD channel as well as the *K2* CCD images of their aperture masks used by EVEREST with Pan-STARRS images to search for stellar contaminants within

⁴ Available at https://archive.stsci.edu/k2/ffi_display.php

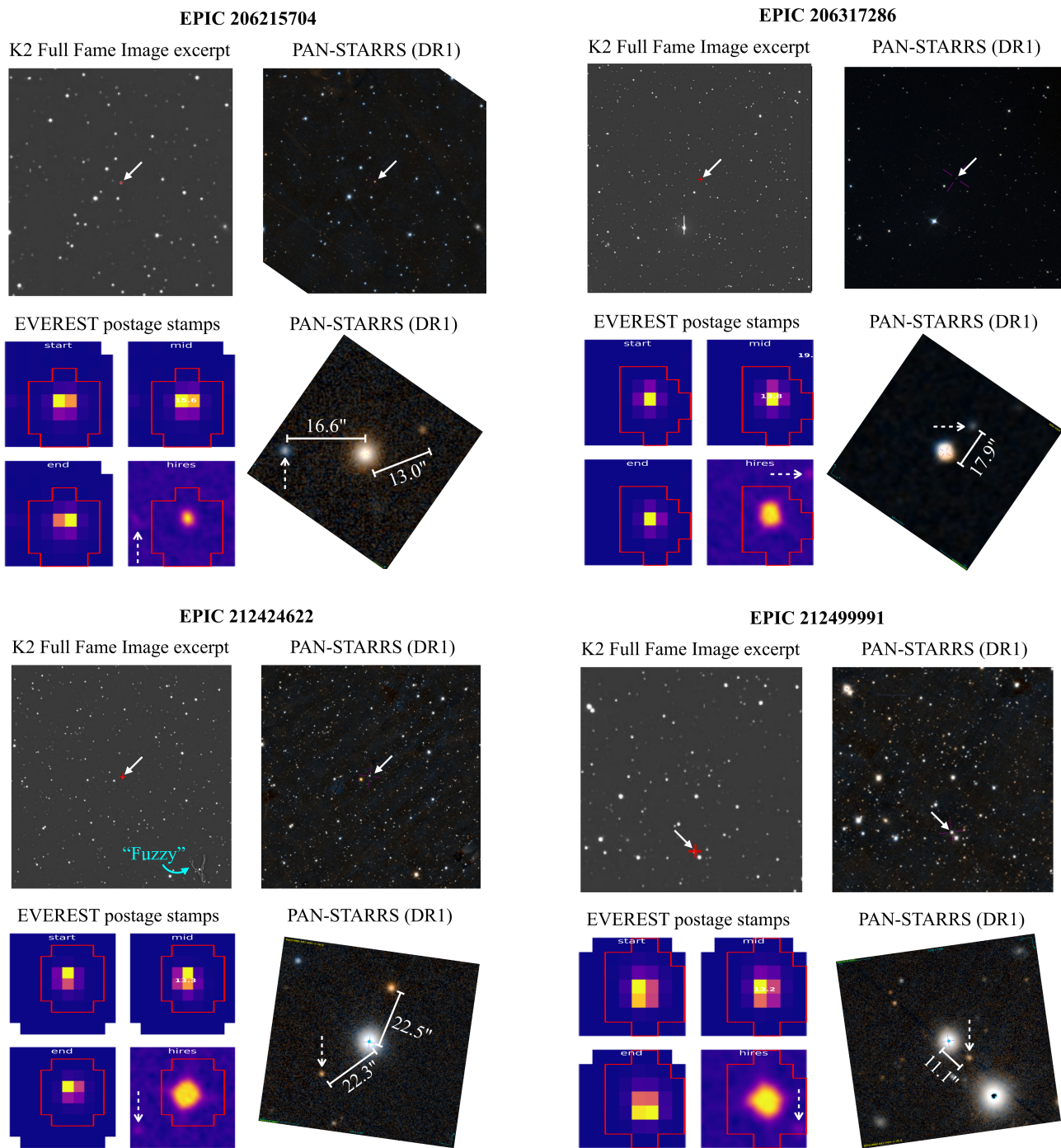


Fig. 2. Comparison of K2 CCD Full Frame Images, K2 aperture masks used by EVEREST, and high-resolution Pan-STARRS (DR1) images for EPIC 206215704 (top left), EPIC 206317286 (top right), EPIC 212424622 (bottom left), and EPIC 212499991 (bottom right). For each of the four objects, four panels show in a clockwise direction the K2 CCD Full Frame Image, the Pan-STARRS image, a Pan-STARRS image zoom, and the EVEREST postage stamps with the pixel map of the aperture mask outlined in red. Solid arrows mark the positions of our targets. Dashed arrows indicate nearby sources that we examined as possible contaminants. “Fuzzy” is labeled and marked with a curved light blue arrow.

the respective apertures. In Fig. 2 we show the corresponding images that we inspected for EPIC 206215704 (top left), EPIC 206317286 (top right), EPIC 212424622 (bottom left)⁵, and EPIC 212499991 (bottom right) as examples. Initial examination of the Pan-STARRS images suggested the presence

of nearby possible stellar contaminants to these objects, but the comparison with the correctly oriented K2 postage stamps⁶ showed that they are outside of the respective aperture masks of EPIC 206215704, EPIC 206317286, and EPIC 212424622. In these cases we concluded that no contaminant is optically re-

⁵ A structure nicknamed “Fuzzy” that was likely caused by a piece of fabric on the CCD when collecting laboratory-based data for the flat-field correction (Doug Caldwell & Geert Barentsen, priv. comm.) is labeled and marked with a curved light blue arrow.

⁶ Available on the Data Validation Summary through the python implementation of EVEREST via `>import everest` `>everest.DVS(206215704)`

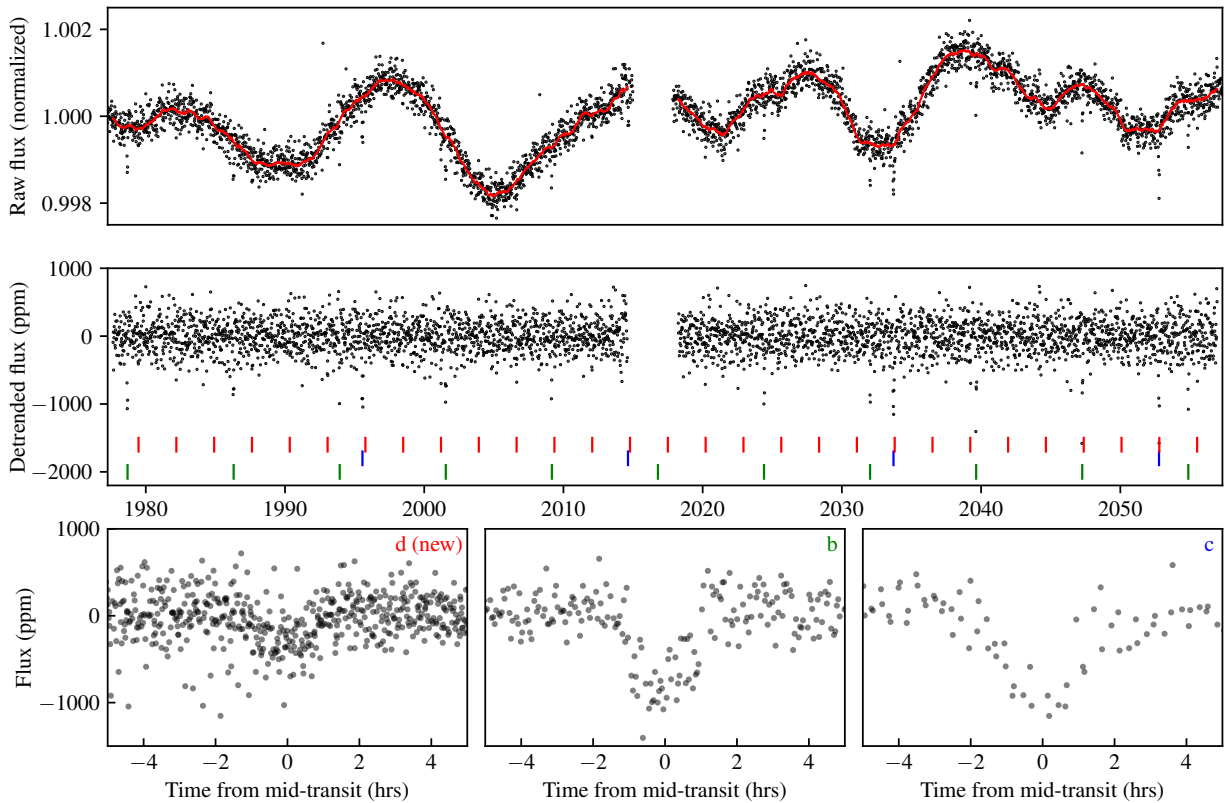


Fig. 3. Example of our detrending of a *K2* light curve and successive transit detection with TLS using the data of *K2*-16 (EPIC 201754305). *Top*: EVEREST light curve (black dots) and our running median filter (red line). *Center*: Detrended light curve that we used as an input to TLS. Transit times of the previously known planets *K2*-16 b and c are marked with green and blue vertical bars, respectively. Transit times of the newly discovered planet *K2*-16 d are indicated with red vertical bars. *Bottom*: Phase-folded transit light curves of all three planets sorted by increasing orbital period from left to right: *K2*-16 d, b, and c.

solved from the three targets and that the measured flux must have been produced within the respective point spread functions ($\rho = 1''$) of the targets within the corresponding Pan-STARRS images. In the fourth case of EPIC 212499991, we found indeed that the candidate contaminant is within the *K2* aperture mask used by EVEREST. The apparent separation between the target and this nearby source is $\rho = 11.1''$, and *vespa* predicted an FPP of 2×10^{-1} .

We here present only objects for which we derived an FPP lower than 1%. We designate these objects as “statistically validated” exoplanets. As a consequence, with an FPP = 2×10^{-1} EPIC 212499991 cannot be validated with *vespa* and our constraints on the possibility of nearby contaminants. We can, however, make use of the “multiplicity boost” factor (X_2) that is implied by the presence of two planet candidates within the same aperture. These candidates have much lower FPPs than single candidates (Lissauer et al. 2012). We computed the multiplicity-corrected FPP for a second planet (FPP₂) from the probability of planethood in a two-planet system (P_2) as $\text{FPP}_2 = 1 - P_2$, where

$$P_2 \approx \frac{X_2 P_1}{X_2 P_1 + (1 - P_1)}, \quad (1)$$

with $P_1 = 1 - \text{FPP}$ and $X_2 = 25$, as estimated by both Lissauer et al. (2012) and Sinukoff et al. (2016). For any system in which we detected a third transiting candidate rather than a second, the multiplicity boost is even stronger and the resulting FPP for that specific object is lower than the values that we present.

In the case of EPIC 212499991, the multiplicity boost derived with Eq. (1) pushed the transit candidate below the validation threshold with an $\text{FPP}_2 = 9.9 \times 10^{-3}$. All other planets in our sample were found to have substantially lower FPP₂ values.

2.5. System characterization with MCMC fitting

As in Paper I, we used the MCMC sampler *emcee* (Foreman-Mackey et al. 2013) to constrain the planetary parameters. In brief, we provided *emcee* with the times of the mid-points of the first transit (T_1) and with the orbital period (P) as measured with TLS for each planet in a given system. For each planet, P , T_1 , the planet-to-star radius ratio ($r_p = R_p/R_s$) and the transit impact parameter (b) were free model parameters, whereas the stellar density (ρ_s) and the two limb-darkening coefficients (according to the quadratic limb-darkening law of Kipping 2013) were global parameters for all transits in a given light curve. Each of the 100 MCMC walkers applied to a light curve executed 200,000 steps, the first half of which we neglected to only preserve burned-in MCMC chains.

We measured the time of mid-transit of the first transit after the center of the respective *K2* light curve for a given object, $T_0 = \text{BKJD} - 2065 \text{ d}$, where the Barycentric Kepler Julian Day is $\text{BKJD} = \text{BJD} - 2,454,833.0 \text{ d}$. This value minimizes the error in T_0 and it minimizes the correlation between T_0 and P .

To deduce the errors (σ_{R_p}) of the planetary radii $R_p = r_p R_s$, we propagated the respective error of the stellar radius (σ_{R_s}) reported in the literature and the error in the planet-to-star radius

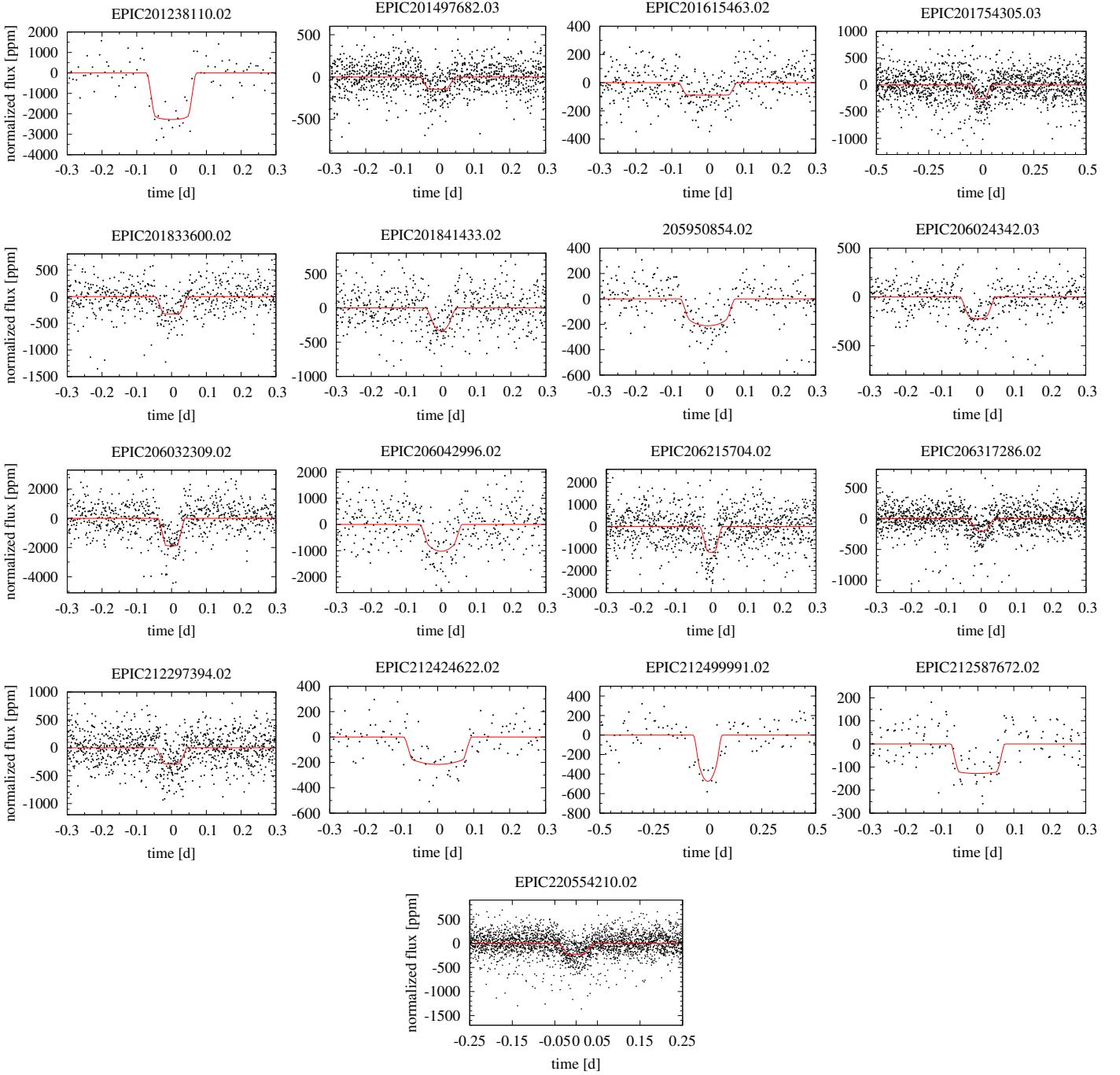


Fig. 4. Gallery of the phase-folded transit light curves for each of the 17 newly discovered planets.

ratio obtained with our MCMC fitting (σ_{r_p}) through a first-order Taylor series expansion,

$$\sigma_{R_p} = \sqrt{(\partial R_p / \partial r_p)^2 \sigma_{r_p}^2 + (\partial R_p / \partial R_s)^2 \sigma_{R_s}^2} = \sqrt{R_s^2 \sigma_{r_p}^2 + r_p^2 \sigma_{R_s}^2}. \quad (2)$$

3. Results

Our initial search in the 489 light curves revealed 50 new candidates that fulfilled our automated search criteria. For each candidate, we then inspected the respective vetting sheet by eye and thereby reduced the number of candidates to 20. We then inspected the *K2* aperture masks used by EVEREST and compared

them to high-resolution images from Pan-STARRS to evaluate the apparent separation of any possible contaminants. The resulting characterization was then submitted to *vespa* for the calculation of the respective FPPs. This chain of successive vetting criteria resulted in the detection and statistical validation of 17 hitherto undetected planets.

Figure 3 shows an example of our iterative transit search with TLS that led us to the discovery of K2-16d (EPIC 201754305.03). The top panel presents the *K2* light curve extracted with EVEREST and the running median indicated with a red line, the center panel shows the detrended light curve used for the transit search with TLS, and the three panels at the bottom illustrate the phase-folded light curves obtained from the re-

Table 1. Characterization and validation of the 17 new planets from our TLS search, MCMC fitting, and vespa false-positive vetting pipeline.

EPIC	K2 name	$M_s [M_\odot]$	$T_0^{(a)}$	P [d]	R_p/R_s	$R_p [R_\oplus]$	b	#tr ^(b)	SNR	SDE _{TLS}	ρ [']	FPP	FPP ₂
201238110.02 ^(d)		$0.410^{+0.112}_{-0.048}$	$-45.3428^{+0.0023}_{-0.0023}$	$28.1656^{+0.0027}_{-0.0028}$	$0.0458^{+0.0021}_{-0.0022}$	$1.87^{+0.20}_{-0.45}$	$0.24^{+0.24}_{-0.17}$	3	12.1	27.5	1.0	5.3×10^{-4}	2.1×10^{-5}
201497682.03 ^(d)		$0.780^{+0.085}_{-0.170}$	$-47.9737^{+0.0028}_{-0.0026}$	$2.13174^{+0.00022}_{-0.00022}$	$0.0115^{+0.0008}_{-0.0008}$	$0.692^{+0.059}_{-0.048}$	$0.21^{+0.23}_{-0.15}$	36	9.5	21.2	22.3	5.0×10^{-2}	2.1×10^{-3}
201615463.02 ⁽ⁱ⁾	K2-166	$1.073^{+0.034}_{-0.034}$	$723.2227^{+0.0051}_{-0.0053}$	$3.80464^{+0.00091}_{-0.00105}$	$0.0093^{+0.0007}_{-0.0007}$	$1.22^{+0.21}_{-0.17}$	$0.61^{+0.14}_{-0.15}$	15	8.0	17.7	24.1	1.7×10^{-2}	6.8×10^{-4}
201753305.03 ^(cde)	K2-16	$0.670^{+0.030}_{-0.040}$	$-47.5037^{+0.0029}_{-0.0029}$	$2.71578^{+0.00031}_{-0.00031}$	$0.015^{+0.001}_{-0.001}$	$1.03^{+0.085}_{-0.086}$	$0.21^{+0.21}_{-0.14}$	26	9.6	22.9	0.5	3.2×10^{-5}	1.3×10^{-6}
201833600.02 ^(de)	K2-50	$0.611^{+0.056}_{-0.056}$	$-45.3448^{+0.0025}_{-0.0025}$	$3.96151^{+0.00046}_{-0.00051}$	$0.0168^{+0.0012}_{-0.0012}$	$1.00^{+0.12}_{-0.11}$	$0.40^{+0.20}_{-0.24}$	18	8.0	12.7	10.0	8.3×10^{-3}	3.3×10^{-4}
201841433.02 ^(d)		$0.802^{+0.081}_{-0.163}$	$-44.6700^{+0.0037}_{-0.0033}$	$4.16959^{+0.00051}_{-0.00053}$	$0.0160^{+0.0017}_{-0.0016}$	$1.10^{+0.14}_{-0.12}$	$0.36^{+0.25}_{-0.24}$	18	7.3	19.1	1.0	3.8×10^{-3}	1.5×10^{-4}
205950854.02 ^(di)	K2-168	$0.907^{+0.032}_{-0.029}$	$115.9808^{+0.0062}_{-0.0061}$	$8.0468^{+0.0024}_{-0.0025}$	$0.0124^{+0.0010}_{-0.0009}$	$1.18^{+0.13}_{-0.10}$	$0.31^{+0.25}_{-0.21}$	9	10.0	21.3	1.0	2.9×10^{-3}	1.2×10^{-4}
206024342.03 ^(de)		$0.928^{+0.082}_{-0.098}$	$1.1324^{+0.0026}_{-0.0027}$	$4.50756^{+0.00062}_{-0.00060}$	$0.0147^{+0.0012}_{-0.0010}$	$1.70^{+0.59}_{-0.31}$	$0.70^{+0.09}_{-0.10}$	13	11.3	25.1	27.0	2.4×10^{-2}	9.7×10^{-4}
206032309.02 ^(d)		$0.221^{+0.035}_{-0.062}$	$1.1320^{+0.0017}_{-0.0017}$	$2.87814^{+0.00023}_{-0.00026}$	$0.0405^{+0.0024}_{-0.0024}$	$1.01^{+0.24}_{-0.13}$	$0.26^{+0.26}_{-0.18}$	24	11.9	20.7	1.0	8.1×10^{-3}	3.3×10^{-4}
206042996.02 ^(d)		$0.565^{+0.053}_{-0.053}$	$1.1227^{+0.0029}_{-0.0029}$	$5.29711^{+0.00074}_{-0.00070}$	$0.0294^{+0.0018}_{-0.0019}$	$1.62^{+0.17}_{-0.19}$	$0.26^{+0.23}_{-0.18}$	12	9.7	19.7	1.0	8.4×10^{-4}	3.4×10^{-5}
206215704.02 ^(d)		$0.407^{+0.095}_{-0.079}$	$112.0005^{+0.0009}_{-0.0009}$	$2.25372^{+0.00047}_{-0.00047}$	$0.0225^{+0.0022}_{-0.0022}$	$0.90^{+0.19}_{-0.20}$	$0.28^{+0.28}_{-0.20}$	29	12.4	22.5	1.0	1.1×10^{-1}	5.0×10^{-3}
206317286.02 ^(d)		$0.711^{+0.090}_{-0.025}$	$113.3327^{+0.0024}_{-0.0024}$	$1.58252^{+0.00017}_{-0.00018}$	$0.0133^{+0.0014}_{-0.0012}$	$0.96^{+0.11}_{-0.15}$	$0.57^{+0.15}_{-0.24}$	42	10.2	25.2	1.0	1.1×10^{-2}	4.6×10^{-4}
212297394.02 ^(e)		$0.829^{+0.087}_{-0.121}$	$363.4607^{+0.0020}_{-0.0020}$	$2.28943^{+0.00019}_{-0.00019}$	$0.0162^{+0.0010}_{-0.0010}$	$1.323^{+0.081}_{-0.095}$	$0.45^{+0.16}_{-0.21}$	33	11.1	24.2	1.0	4.4×10^{-3}	1.8×10^{-4}
212424622.02 ^(e)		$1.106^{+0.145}_{-0.120}$	$365.2616^{+0.0090}_{-0.0069}$	$18.0983^{+0.0060}_{-0.0058}$	$0.0148^{+0.0013}_{-0.0011}$	$2.17^{+0.67}_{-0.42}$	$0.74^{+0.08}_{-0.07}$	4	8.5	19.0	1.0	2.2×10^{-2}	9.2×10^{-4}
212499991.02 ^(e)		$0.912^{+0.037}_{-0.162}$	$382.6254^{+0.0081}_{-0.0096}$	$34.885^{+0.011}_{-0.010}$	$0.0193^{+0.0016}_{-0.0019}$	$1.60^{+0.13}_{-0.16}$	$0.28^{+0.26}_{-0.19}$	2	9.1	11.9	11.1	2.0×10^{-1}	9.9×10^{-3}
212587672.02 ^{(e)(k)}		$0.950^{+0.040}_{-0.040}$	$375.4906^{+0.0053}_{-0.0054}$	$15.2841^{+0.0037}_{-0.0029}$	$0.0108^{+0.0007}_{-0.0007}$	$1.12^{+0.12}_{-0.09}$	$0.24^{+0.25}_{-0.17}$	5	8.6	18.5	23.5	1.3×10^{-1}	6.1×10^{-3}
220554210.02 ^(dk)	K2-282	$0.940^{+0.040}_{-0.040}$	$532.1411^{+0.0017}_{-0.0017}$	$0.70531^{+0.00005}_{-0.00005}$	$0.0146^{+0.0007}_{-0.0007}$	$1.48^{+0.13}_{-0.10}$	$0.25^{+0.24}_{-0.17}$	103	16.8	25.8	1.0	4.0×10^{-5}	1.6×10^{-6}

Notes. T_0 , P , R_p/R_s , and b obtained from MCMC fitting. #tr, S/N, and SDE_{TLS} obtained from TLS. FPP₂ obtained with vespa and corrected for the multiplicity boost following Eq. (1). $R_p [R_\oplus]$ derived from R_p/R_s as per TLS and literature values for the stellar radius. All stellar radii and masses from Huber et al. (2016), except for EPIC201497682⁽ⁱ⁾, EPIC201615463⁽ⁱ⁾, EPIC201754305^(d), EPIC201841433⁽ⁱ⁾, EPIC205950854⁽ⁱ⁾, EPIC212297394⁽ⁱ⁾, EPIC212499991⁽ⁱ⁾, EPIC212587672^(k), and EPIC220554210^(k).

^(a) $T_0 = \text{BJD} - 2065$ d with the Barycentric Kepler Julian Day $\text{BJD} = \text{BJD} - 2,454,833.0$ d.

^(b) Number of transits detected with TLS that have data.

Planets or candidates have previously been found in these systems by ^(c) Montet et al. (2015), ^(d) Vanderburg et al. (2016), ^(e) Barros et al. (2016), ^(f) Crossfield et al. (2016), ^(g) Pope et al. (2016), ^(h) Dressing et al. (2017), ⁽ⁱ⁾ Mayo et al. (2018), ^(j) Livingston et al. (2018a), ^(k) Pettigura et al. (2018).

Gaia DR2 radii were computed by ^(l) Andrae et al. (2018).

spective T_0 and P values detected with TLS for each of the three planets. The new planet is shown in the bottom left panel.

The final sample of 17 validated planets was then characterized with the emcee MCMC sampler. The results are listed in Table 1 including T_0 , P , R_p/R_s , and b . Table 1 also summarizes the characteristics of the $K2$ light curves as evaluated with TLS, such as the number of detected transits for the new object ($\#tr$), S/N, and SDE_{TLS} as well as the quantities ρ , FPP, and FPP_2 that relate to the *vespa* software.

In Fig. 4 we present a gallery of the phase-folded transits of all 17 newly discovered transiting planets. Each panel contains the detrended and phase-folded $K2$ light curve (black dots) and our best fit obtained through the MCMC sampling of the data (red line). The scales of the ordinates are different in the panels, which show transit depths ranging from about 100 ppm (EPIC 201615463.02) to more than 2000 ppm (EPIC 201238110.02). The very shallow depths of these phase-folded light curves, with S/Ns just between about 7 and 17 (see Table 1), make it very hard for the human eye to classify the morphologies of the transit light curves as either box-like, transit-like, or V-shaped, etc. The question then arises why TLS finds these noisy transits but previous studies that used box-fitting algorithms missed them. We have previously investigated this question and found three answers. First, TLS is intrinsically more sensitive to shallow transits simply because it uses a more physical description of a transit light curve. This fact tends to produce higher SDE values for real planets and lower SDE values for false positives (Hippke & Heller 2019). Second, and different from the vast majority of BLS implementations, the grid of trial periods used in TLS is not linear. Instead, the grid of trial orbital frequencies is linear, which makes TLS equally sensitive to short- and long-period transiting planets while minimizing the computational load (Ofir 2014). This suppresses the occurrence of aliases and false positives (Paper I). Third, in Paper I we showed that the Earth-sized planet K2-32 e can indeed be found with BLS in the $K2$ data that were detrended from systematic effects by the EVEREST pipeline, whereas previous studies used the slightly more noisy K2SFF light curves (Vanderburg & Johnson 2014).

Figure 5 is an illustration of the orbital architectures of the 17 systems with new planets. In each panel, we show the respective host star at the left and indicate its effective temperature by a color (see caption). Each panel shows all planets that are now known around these 17 stars. The positions of the planets are based on their transit impact parameters (along the ordinate) and orbital semi-major axes (a , along the abscissa) derived from our MCMC modeling of the entire light curve. For our estimations of a , we assumed Kepler's third law for circular orbits and neglected the planetary masses, $a = (GM_s(P/2\pi)^2)^{1/3}$, where G is the gravitational constant. In each panel, the abscissa ranges from 0 to 0.2 AU and the ordinate extends to one solar radius. All symbols are to scale with respect to the sizes of all objects shown.

In 11 out of 17 cases, the new planet that we found is now the innermost known planet in its system. In 13 out of 17 cases, the new planet is the smallest of the known planets in its system. In the remaining four cases, in which the new planet is not the smallest planet, it is the outermost of the known planets and therefore shows the smallest number of transits and, hence, the lowest SDE_{TLS} in this system.

In the period-radius diagram shown in Fig. 6 we place our sample of 17 new planets from $K2$ in the broader context of the known population of transiting exoplanets. Different symbols denote planets from different samples. Open circles denote

transiting planets that are not from $K2$, and thus mostly from the *Kepler* primary mission, blue circles refer to planet known from $K2$, and red circles depict planets from $K2$ that were found by the TLS Survey. The first statistically validated planet from the TLS Survey, K2-32 e (Paper I), is denoted with an orange circle. Figure 6 translates the enhanced sensitivity of TLS compared to BLS for shallow transits, as found in simulations by Hippke & Heller (2019), into the exoplanet period-radius diagram.

All of the new planets, except for one object that orbits a star larger than the sun, are smaller than two Earth radii, and as a consequence, produce very shallow transits. As shown in Paper I for the case of K2-32 e, these transits can be very close to the detection limit for a heuristically chosen SDE in BLS (SDE_{BLS}), but they can exceed an equivalent detection limit chosen for TLS to produce the same false-positive rates (Hippke & Heller 2019). Consequently, we verify that TLS is particularly suited for the search of small planets. The most remarkable object in terms of its small size is EPIC 201497682.03, which we found to have a radius of just $0.692^{+0.059}_{-0.048} R_{\oplus}$, making it the second smallest planet ever discovered with $K2$. Another highlight is the super-Earth EPIC 201238110.02, which orbits its M dwarf host star in the habitable zone (Kopparapu et al. 2013). This means it could potentially have liquid surface water, although we expect that the strong tidal forces from the star have aligned the spin with the orbit and therefore eroded any seasons on the planet (Heller et al. 2011).

4. Discussion

The ability of TLS to find hitherto unknown planets in the short-period Earth-sized regime (see Fig. 6) is so high that a dedicated TLS-based transit search has the potential of extending previous work on ultra-short-period planets (Jackson et al. 2013; Sanchis-Ojeda et al. 2014; Adams et al. 2016). Short-period planets are particularly interesting from a planet-formation point of view, in particular in the context of the curious planet radius gap (Fulton et al. 2017) and the stability of planetary atmospheres under extreme stellar irradiation (Lehmer & Catling 2017). Small, ultra-short-period planets are also interesting in terms of their connection to stellar metallicity (Winn et al. 2017) and with regard to their tidal interaction with the star (Barnes 2015).

A reanalysis of light curves that have previously been searched for with BLS or similar algorithms is very likely to reveal new ultra-short-period Earth-sized planets. Our discovery rate of 18 newly validated planets (including K2-32 e; Paper I) around 489 stars with previously known planets ($18/489 \approx 3.7\%$) suggests the potential for the discovery of another roughly 100 additional planets in the data of the thousands of stars with planets and candidates from the *Kepler* primary mission. The numbers might be even higher given that the light curves from the *Kepler* primary mission contain four years of continuous observations compared to the approximately 80 d covered by $K2$. Moreover, follow-up transit searches with TLS can be used to validate known planet candidates by using the multiplicity boost in case of additional candidate detections, as done in this study.

5. Conclusions

We reported the discovery of 17 new planets in the archival data of the extended *Kepler* mission, $K2$. All of these planets are smaller than about $2.2 R_{\oplus}$, and half of these planets are smaller than about $1.2 R_{\oplus}$. While their extremely shallow transits were

not securely detectable with standard transit-search algorithms looking for box-like transit signals, our newly developed TLS transit search algorithm (Hippke & Heller 2019) identified them as transiting candidates.

We used the *vespa* software and optical images from Pan-STARRS to statistically validate these candidates with $FPP < 1\%$. Our characterization of these validated exoplanets based on an MCMC analysis of their entire *K2* light curves with the *emcee* software reveals that one of our objects, EPIC 201497682.03, with a radius of $0.692^{+0.059}_{-0.048} R_{\oplus}$ is now the second smallest planet ever discovered with *K2*.

Based on our discovery rate of one new planet around about 3.7% of all stars from *K2* with previously known planets, we expect that TLS can find another 100 small planets around the thousands of stars with planets and candidates from the *Kepler* primary mission that have been missed in previous searches.

Acknowledgements. The authors thank an anonymous referee for their comments that helped to clarify several passages in this manuscript. This research has made use of the Exoplanet Orbit Database and the Exoplanet Data Explorer at exoplanets.org. This research has made use of the NASA Exoplanet Archive, which is operated by the California Institute of Technology, under contract with the National Aeronautics and Space Administration under the Exoplanet Exploration Program. This work made use of NASA's ADS Bibliographic Services. This research has made use of "Aladin sky atlas" developed at CDS, Strasbourg Observatory, France. The Pan-STARRS1 Surveys (PS1) and the PS1 public science archive have been made possible through contributions by the Institute for Astronomy, the University of Hawaii, the Pan-STARRS Project Office, the Max-Planck Society and its participating institutes, the Max Planck Institute for Astronomy, Heidelberg and the Max Planck Institute for Extraterrestrial Physics, Garching, The Johns Hopkins University, Durham University, the University of Edinburgh, the Queen's University Belfast, the Harvard-Smithsonian Center for Astrophysics, the Las Cumbres Observatory Global Telescope Network Incorporated, the National Central University of Taiwan, the Space Telescope Science Institute, the National Aeronautics and Space Administration under Grant No. NNX08AR22G issued through the Planetary Science Division of the NASA Science Mission Directorate, the National Science Foundation Grant No. AST-1238877, the University of Maryland, Eotvos Lorand University (ELTE), the Los Alamos National Laboratory, and the Gordon and Betty Moore Foundation. This work has made use of data from the European Space Agency (ESA) mission *Gaia* (www.cosmos.esa.int/gaia), processed by the *Gaia* Data Processing and Analysis Consortium (DPAC, www.cosmos.esa.int/web/gaia/dpac/consortium). Funding for the DPAC has been provided by national institutions, in particular the institutions participating in the *Gaia* Multilateral Agreement. RH is supported by the German space agency (Deutsches Zentrum für Luft- und Raumfahrt) under PLATO Data Center grant 50001501. KR is a member of the International Max Planck Research School for Solar System Science at the University of Göttingen. KR performed the MCMC analysis of the light curves.

References

Adams, E. R., Jackson, B., & Endl, M. 2016, *AJ*, 152, 47
 Aigrain, S. & Favata, F. 2002, *A&A*, 395, 625
 Aigrain, S., Hodgkin, S. T., Irwin, M. J., Lewis, J. R., & Roberts, S. J. 2015, *MNRAS*, 447, 2880
 Aigrain, S. & Irwin, M. 2004, *MNRAS*, 350, 331
 Aigrain, S., Parviainen, H., & Pope, B. J. S. 2016, *MNRAS*, 459, 2408
 Akeson, R. L., Chen, X., Ciardi, D., et al. 2013, *Publications of the Astronomical Society of the Pacific*, 125, 989
 Andrae, R., Fousneau, M., Creevey, O., et al. 2018, *A&A*, 616, A8
 Armstrong, D. J., Günther, M. N., McCormac, J., et al. 2018, *MNRAS*, 478, 4225
 Barnes, R. 2015, *International Journal of Astrobiology*, 14, 321
 Barros, S. C. C., Demangeon, O., & Deleuil, M. 2016, *A&A*, 594, A100
 Bordé, P., Fressin, F., Ollivier, M., Léger, A., & Rouan, D. 2007, in *Transiting Extrapolar Planets Workshop*, Vol. 366, 145
 Borucki, W. J., Koch, D., Basri, G., et al. 2010, *Science*, 327, 977
 Bouffleur, R. C., Emilio, M., Pacheco, E. J., de La Reza, J. R., & da Rocha, J. C. 2014, in *Formation, Detection, and Characterization of Extrasolar Habitable Planets*, Vol. 293, 410–412
 Cabrera, J., Csizmadia, S., Erikson, A., Rauer, H., & Kirste, S. 2012, *A&A*, 548, A44
 Carter, J. A. & Agol, E. 2013, *ApJ*, 765, 132

Chambers, K. C., Magnier, E. A., Metcalfe, N., et al. 2016, arXiv e-prints, arXiv:1612.05560
 Collier Cameron, A., Pollacco, D., Street, R. A., et al. 2006, *MNRAS*, 373, 799
 Crossfield, I. J. M., Ciardi, D. R., Petigura, E. A., et al. 2016, *ApJS*, 226, 7
 Crossfield, I. J. M., Guerrero, N., David, T., et al. 2018, *ApJS*, 239, 5
 Crossfield, I. J. M., Petigura, E., Schlieder, J. E., et al. 2015, *ApJ*, 804, 10
 Cutri, R. M., Skrutskie, M. F., van Dyk, S., et al. 2003, *VizieR Online Data Catalog*, 2246
 Deming, D., Knutson, H., Kammer, J., et al. 2015, *ApJ*, 805, 132
 Dressing, C. D., Vanderburg, A., Schlieder, J. E., et al. 2017, *AJ*, 154, 207
 Foreman-Mackey, D., Hogg, D., Lang, D., & Goodman, J. 2013, *PASP*, 125, 306
 Foreman-Mackey, D., Montet, B. T., Hogg, D. W., et al. 2015, *ApJ*, 806, 215
 Fulton, B. J., Petigura, E. A., Howard, A. W., et al. 2017, *AJ*, 154, 109
 Gaia Collaboration, Brown, A. G. A., Vallenari, A., et al. 2018, *A&A*, 616, A1
 Gaia Collaboration, Prusti, T., de Bruijne, J. H. J., et al. 2016, *A&A*, 595, A1
 Gaidos, E., Mann, A. W., Rizzuto, A., et al. 2017, *MNRAS*, 464, 850
 Giles, H. A. C., Osborn, H. P., Blanco-Cuaresma, S., et al. 2018, *A&A*, 615, L13
 Han, E., Wang, S. X., Wright, J. T., et al. 2014, *PASP*, 126, 827
 Heller, R., Leconte, J., & Barnes, R. 2011, *A&A*, 528, A27
 Heller, R., Rodenbeck, K., & Hippke, M. 2019, *A&A*, 625, A31
 Hippke, M. & Heller, R. 2019, *A&A*, 623, A39
 Howell, S. B., Sobek, C., Haas, M., et al. 2014, *Publications of the Astronomical Society of the Pacific*, 126, 398
 Huber, D., Bryson, S. T., Haas, M. R., et al. 2016, *The Astrophysical Journal Supplement Series*, 224, 2
 Jackson, B., Stark, C. C., Adams, E. R., Chambers, J., & Deming, D. 2013, *ApJ*, 779, 165
 Jenkins, J. M., Doyle, L. R., & Cullers, D. K. 1996, *Icarus*, 119, 244
 Kipping, D. M. 2013, *MNRAS*, 435, 2152
 Kopparapu, R. K., Ramirez, R., Kasting, J. F., et al. 2013, *ApJ*, 765, 131
 Kovács, G., Zucker, S., & Mazeh, T. 2002, *A&A*, 391, 369
 Lehmer, O. R. & Catling, D. C. 2017, *ApJ*, 845, 130
 Lissauer, J. J., Marcy, G. W., Rowe, J. F., et al. 2012, *ApJ*, 750, 112
 Livingston, J. H., Crossfield, I. J. M., Petigura, E. A., et al. 2018a, *AJ*, 156, 277
 Livingston, J. H., Endl, M., Dai, F., et al. 2018b, *AJ*, 156, 78
 Luger, R., Agol, E., Kruse, E., et al. 2016, *AJ*, 152, 100
 Lund, M. N., Handberg, R., Davies, G. R., Chaplin, W. J., & Jones, C. D. 2015, *ApJ*, 806, 30
 Mandel, K. & Agol, E. 2002, *ApJ*, 580, L171
 Mann, A. W., Newton, E. R., Rizzuto, A. C., et al. 2016, *AJ*, 152, 61
 Mayo, A. W., Vanderburg, A., Latham, D. W., et al. 2018, *AJ*, 155, 136
 Mislis, D., Bachelet, E., Alsubai, K. A., Bramich, D. M., & Parley, N. 2016, *MNRAS*, 455, 626
 Montet, B. T., Morton, T. D., Foreman-Mackey, D., et al. 2015, *ApJ*, 809, 25
 Morton, T. D. 2012, *ApJ*, 761, 6
 Morton, T. D. 2015, *VESPA: False positive probabilities calculator*, *Astrophysics Source Code Library*
 Ofir, A. 2014, *A&A*, 561, A138
 Osborn, H. P., Armstrong, D. J., Brown, D. J. A., et al. 2016, *MNRAS*, 457, 2273
 Pearson, K. A., Palafox, L., & Griffith, C. A. 2018, *MNRAS*, 474, 478
 Petigura, E. A., Crossfield, I. J. M., Isaacson, H., et al. 2018, *AJ*, 155, 21
 Petigura, E. A. & Marcy, G. W. 2012, *PASP*, 124, 1073
 Petigura, E. A., Marcy, G. W., & Howard, A. W. 2013, *ApJ*, 770, 69
 Pont, F., Zucker, S., & Queloz, D. 2006, *MNRAS*, 373, 231
 Pope, B. J. S., Parviainen, H., & Aigrain, S. 2016, *MNRAS*, 461, 3399
 Régulo, C., Almenara, J. M., Alonso, R., Deeg, H., & Roca Cortés, T. 2007, *A&A*, 467, 1345
 Renner, S., Rauer, H., Erikson, A., et al. 2008, *A&A*, 492, 617
 Sanchis-Ojeda, R., Rappaport, S., Winn, J. N., et al. 2014, *ApJ*, 787, 47
 Schmitt, J. R., Tokovinin, A., Wang, J., et al. 2016, *AJ*, 151, 159
 Schwarzenberg-Czerny, A. & Beaulieu, J. P. 2006, *MNRAS*, 365, 165
 Sinukoff, E., Howard, A. W., Petigura, E. A., et al. 2016, *ApJ*, 827, 78
 Tingley, B. 2003a, *A&A*, 403, 329
 Tingley, B. 2003b, *A&A*, 408, L5
 van Sluijs, L. & Van Eylen, V. 2018, *MNRAS*, 474, 4603
 Vanderburg, A. & Johnson, J. A. 2014, *PASP*, 126, 948
 Vanderburg, A., Latham, D. W., Buchhave, L. A., et al. 2016, *The Astrophysical Journal Supplement Series*, 222, 14
 Winn, J. N., Sanchis-Ojeda, R., Rogers, L., et al. 2017, *AJ*, 154, 60
 Yu, L., Crossfield, I. J. M., Schlieder, J. E., et al. 2018, *AJ*, 156, 22
 Zechmeister, M. & Kürster, M. 2009, *A&A*, 496, 577
 Zink, J. K., Hardegree-Ullman, K. K., Christiansen, J. L., et al. 2019, *Research Notes of the American Astronomical Society*, 3, 43
 Zucker, S. & Giryès, R. 2018, *AJ*, 155, 147

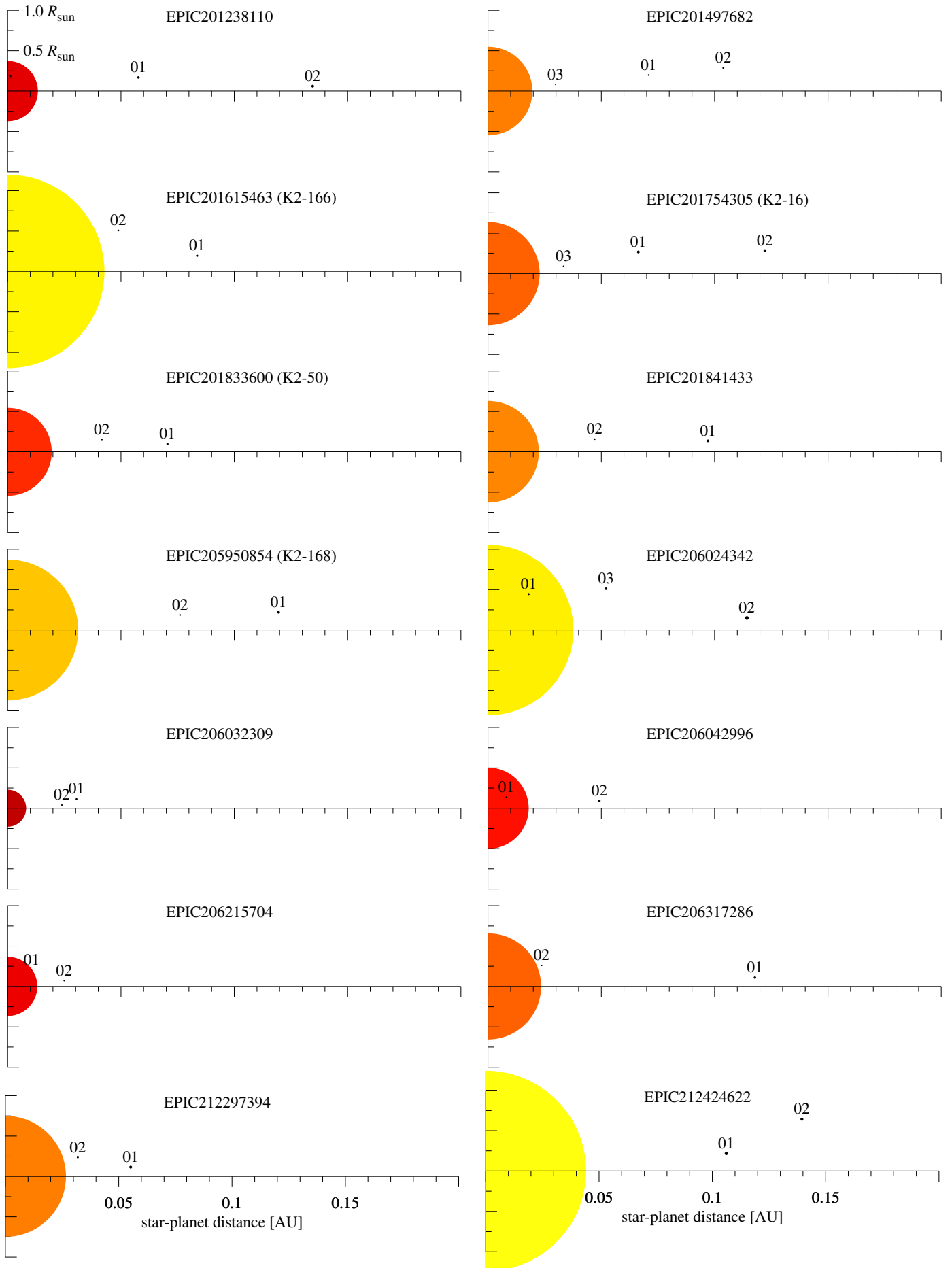


Fig. 5. (continued on next page)

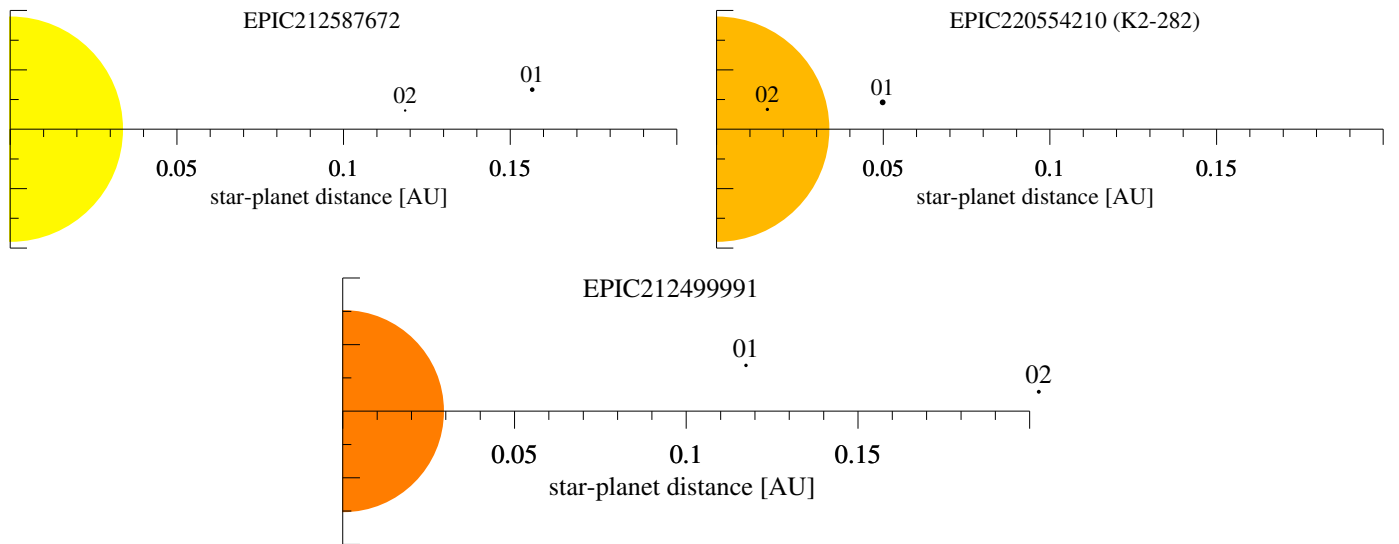


Fig. 5. Orbital architectures of the 17 systems with new planets. The colors of the stars indicate their effective temperatures, ranging from 3500 K (red) to 6100 K (yellow). All planets known in each system are shown, where the new planets are designated with the highest number (02 or 03) in each system. The positions of the planets are chosen based on the results of our MCMC fitting of the entire *K2* light curves, with the x coordinate corresponding to the star-planet distance (in AU) and the y coordinate relating to the transit impact parameter. The ordinate runs from zero to the radius of the Sun. All stellar and planetary radii are to scale. Star-planet distances are also to scale, but radii are not to scale with distances.

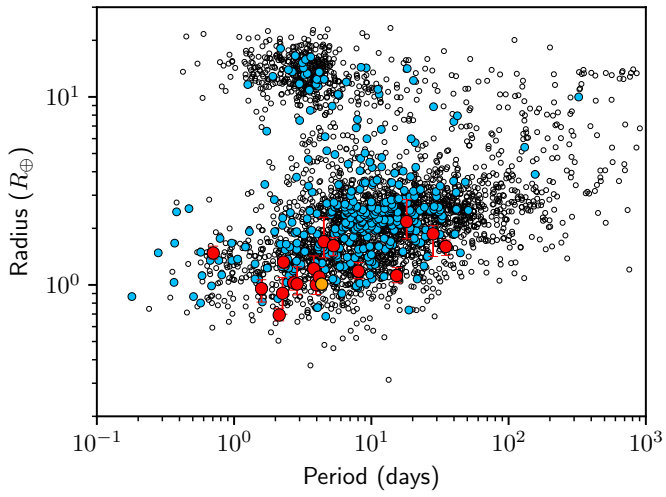


Fig. 6. Period-radius diagram of all confirmed transiting exoplanets (empty circles) mostly from K1, candidates and confirmed planets from K2 (blue), and from the TLS Survey (red), including K2-32 e (orange) presented in [Paper I](#). The uncertainties in the orbital periods of the 18 planets discovered and characterized in the TLS Survey are much smaller and shorter than the symbol size.